2017

Characteristics of Hydrogel-Wetted Thin Films

James Owens
University of Central Florida

CHARACTERISTICS OF HYDROGEL-WETTED
THIN FILMS

by

JAMES FRANCIS OWENS
B.S. University of Central Florida, 2015

A thesis submitted in partial fulfillment of the requirements
for the degree of Master of Science
in the Department of Mechanical and Aerospace Engineering
in the College of Engineering and Computer science
at the University of Central Florida
Orlando, Florida

Spring Term
2017

Major Professor: Shawn A. Putnam

ABSTRACT

The meniscus region of a thin film is known to have high heat transfer properties due to high evaporation rates and activation of latent heat. The region known as the thin film meniscus ($\delta_{film} < 2 \, \mu m$) can account for more than half of the total heat transfer of a droplet or film. This study focuses on the potential elongation and curvature amplification of the thin film meniscus region by the implementation of a layer of high hydrogen bonding (hydrogel) film on which the liquid meniscus is built. Forced wetting via liquid propagation though this hydrogel layer in the radial direction increases the surface area of the film. By analyzing the mass flux of liquid lost through evaporation and using both spectroscopic and optical methods to obtain the curvature of the film, relationships between hydrogel thickness and the resulting mass flux were made. Isothermal and steady state assumptions were used to relate hydrogel thickness layers to meniscus curvature, evaporative mass flux, and overall heat transfer coefficients. The experimental results demonstrate, that steady state conditions are achievable with small percentage change in film profile over time. These results are promising toward the addition of the hydrogel coatings and further advancements in heat piping and high heat flux cooling systems for micro electronic devices.

ACKNOWLEDGMENTS

I would like to first express my profound gratitude to Dr. Shawn A. Putnam for his unwavering support throughout my graduate studies and research. His guidance, teachings, and encouragement were invaluable me and tantamount to my success as an aspiring engineer. I, along with all the students working in his laboratory, have witnessed the effects of his work ethic on not only the whole of laboratory, but on us individually. I have become a better engineer, student, and man having worked under Dr. Putnam and for this I am humbly thankful. I look forward to any and all potential events and collaborations with him in the future as I move from academia into the professional setting at Lockheed Martin.

I must acknowledge Armando Arends for his unrelenting hard work in the lab with me on the set up of this measurement rig. Without him and Dr. Putnam, the work detailed within this thesis would not be possible. Also, I would like to thank Thomas Germain, whom has gladly set down his work day by day to assist in the mundane side work as well as the most important aspects of measurements for the sake of helping a fellow lab mate. I must extend my gratitude to Yousef Almahdi his indispensable help in manufacturing the samples used in this experiment. I would also like to thank Dr. Ali Kosar and Ahmad Reza Motezakker for their work with hydrogels that will make the continuation of this research possible.

I would also like to thank my committee members, Dr. Louis Chow and Dr. Yunjun Xu, for their time and support in the multiple semesters leading to now. As their graduate teaching assistant for classes like thermodynamics and orbital mechanics, I was granted an opportunity for funding and the increased capacity to learn and teach these subjects and am greatly thankful for it.

iii

I would also like to thank my lab mates for their communication, steadfastness, and friendship throughout our time together. To Mehrdad Mehrvand, Krishnan Monahran, Tanvir Ahmed Chowdry, and Mateo Gomez, I extend my thanks for such a great experience as well as the knowledge and enjoyment that I received from our daily interactions.

Additional thanks to my family, friends, and classmates; all of whom have made an impact on my work greater than they know. Finally, I would like to thank the Department of Mechanical and Aerospace Engineering for its support, funding, and guidance that have made this journey possible.

TABLE OF CONTENTS

LIST OF FIGURES

LIST OF TABLES

CHAPTER 1: INTRODUCTION

Background

With the advances in computing, micro processing, and lab on a chip devices, the need for cooling systems with high heat transfer capacities has been growing exponentially. The steps taken over the past 40 years to consolidate decades of advances of separate systems into single microelectromechanical systems (MEMS) has created a niche market for high heat flux micro cooling systems. As a cheap and effective cooling method, fans along with solid heat sinks were used to dissipate this excess heat to prevent part burnout, but as these MEMS devices became more powerful and compact, air alone could not provide the convective cooling necessary to support sustained operation. Higher heat transfer rates were readily available through liquid convection and liquid evaporation (latent heat) and were thus utilized into these systems for low cost, reliable excess heat dissipation.

Heat pipes that utilize two phase flow have been at the fore front of heat transport application in cooling micro electronic devices. In these two-phase heat pipes, fluid is introduced to a heating section and is converted to vapor, either by boiling or evaporating, and then transported to the cold interface where is it condensed back into a fluid, thus releasing the latent heat. In these heat pipes, the heating section corresponds to the section of the pipe that is in contact with the microelectronic component that requires cooling while the cold section is generally exposed to outside conditions of much lower temperatures such as a wall separating the inside of the MEMS to the ambient conditions of the room. The limiting factor of these heat pipes is the length of the heating section in which the fluid is present in two phases (liquid and vapor). This length, called

1

the working length, is the regime where latent heat is activated through evaporation leading to large heat transfer coefficients and high cooling rates. There are multiple areas of research being conducted in attempts to increase the efficiency, sizing, cooling power, etc. of these heat pipes.

The area of interest of this study is in the region of part dry-out. This is the regime where the flow transitions from two phase (liquid and vapor) to single phase flow (vapor). In this regime, temperature is no longer held constant at the critical temperature of the fluid but unbounded, allowing for large temperature increases leading to temperature induced failures and component destruction. By elongating the two-phase flow regime, total heat transfer can be increased and, under constant power output of the device, the probability of dry-out and subsequent part burnout will be decreased.

As detailed above, dry-out results in part damage and, in some cases, critical system failure, therefore a key problem in high heat flux heat piping presents itself, maintaining two phase flow in the heating section of the heat pipe. By keeping the walls of the heating section completely saturated with fluid, temperature is always bounded by the critical temperature of the fluid. The use of highly wetting fluids inside the heat piping were used to ensure higher fluid coverage of inner heating surface. These highly wetting fluids were incorporated into heat piping but are not completely wetting, meaning that they did not distribute themselves across the surface to maximize air displacement (minimize dry locations), and therefore could be improved on by other means.

Wicking structures, commonly used as pillar arrays, were introduced to these heat pipes to drive the condensed fluid toward the heating section without the use of an external driving mechanism. The use of high wetting fluids inside the pipe with these wick structures made use of

2

a phenomena called capillary driven flow. This flow is defined as the tendency of a fluid to penetrate the wick array using capillary force and is only resisted by viscous forces between the fluid and the wicking structures and surface. The wicking structures were found to greatly decrease the chance of a region drying out due to fluid motion toward dry regions.

There comes a location where the heating section will stop and the fluid will keep traversing via the wicking structures. This is considered a waste of fluid and thus fluid penetration into sections following the heating section should be minimized. Considering all preceding remarks, dry sections immediately following the heating section are not only wanted but signal complete latent heat release and maximum efficiency of cooling system. Therefore, the goal of these micro cooling systems is to present the heating section with one-phase saturated liquid flow with quality 0% and after the heating section is complete, be converted to one-phase vapor flow. This ensures all energy capable of dissipation is absorbed by the fluid in the phase change operation.

As this flow transitions from one-phase to two-phase via boiling, nucleation occurs on the walls leading to bubbles. As these bubbles of vapor coalesce into a vapor column inside the flow, concentric to the heat pipe, increasingly more fluid is converted into vapor. These vapor columns will become vapor slugs and eventually the vapor slug will present an interface where flow ceases to be two phased, and becomes single-phase, superheated vapor. It is imperative that the heating of this single phased superheated vapor ceases shortly after formation as to avoid part burnout. The critical regime of this interface is the thin film meniscus made by the fluid as it contacts the wall. There is a curvature to the vapor slug at the interface of liquid and vapor where fluid will be,

at pseudo steady state, converted to vapor. The evaporation rate of such an interface is not constant but has a well-defined maximum. The thin film meniscus at which the surface tension forces dominate is the area of highest evaporative mass flux and therefore the region of highest heat transfer. Vapor slugs with high curvature present an elongated thin film region resulting in higher heat transfer rates. This region, approximate maximum thickness of one to two microns [1], is the furthest reaching section of the two-phased flow in the x direction and offers the highest heat transfer capacity of the entire cooling mechanism. By increasing the curvature of these films and extending the thin film region of the meniscus, it is possible to greatly increase the effective cooling of these devices without impacting the size, basic function, and cost of the system.

Wicking structures provide a means to deliver the fluid to the meniscus region but are typically at least an order of magnitude taller than the thin-film region of the meniscus limiting the evaporation rates. The degree of wetting (contact angle) of the fluid along the wall of the pipe is generally the limiting factor of the meniscus curvature. The angle of the contact line (θ) is always less than 90 degrees for these cases because the fluid is always wetting, if not nearly completely wetting ($\theta = 0$). There comes a point where, if maximum heat flux is the desired outcome, these wicking structures must end and the fluid must be allowed to form this meniscus.

Research Focus and Motivation

It has been discussed the importance of the thin-film region to high heat flux capacity cooling systems. To increase the thin-film meniscus region for a given fluid would be to increase the cooling capacity of the entire system. The implementation of a hydrogen bond promoting film (hydrogel film) appears to be a promising step toward increasing the curvature and heat flux

capacity of these systems. By depositing a range of these films, it will be possible to characterize the effectiveness of the meniscus profile elongation and determine the optimum thickness needed to ensure maximum curvature of meniscus. However, as these films swell with liquid imbibition, contact line dynamics change which makes analysis more complex. By varying film thickness from tens to several hundred nanometers, these contact line dynamics will be able to be studied so to provide a complete analysis of hydrogel impact on the curvature of wetting films.

CHAPTER 2: LITERATURE REVIEW

Surface Forces and Wetting Phenomena

Wetting of fluids on substrates have been receiving great interest in the academic community for over 200 years. Dating back to 1805 when Thomas Young wrote his essay detailing the relationship between contact angle and interfacial surface forces[2]. To introduce, the measure of the ability of a fluid to displace air on a solid substrate/material is defined as the wettability of that fluid on said substrate/material. In the case of a liquid deposited on a solid substrate, the interface where liquid, vapor, and solid are present is called the "triple-line". The angle between the solid-liquid interface and the liquid-vapor interface extending from the triple line is called the contact angle. The fluid can be said to be highly-wetting, partially-wetting, or non-wetting depending on Young's contact angle (θ)[3]. This contact angle, as shown in Fig. 1, will be small ($\theta \ll 90°$) for fluids that are highly wetting on the substrate, less than 90° for partially wetting, and greater than 90° for non-wetting films.
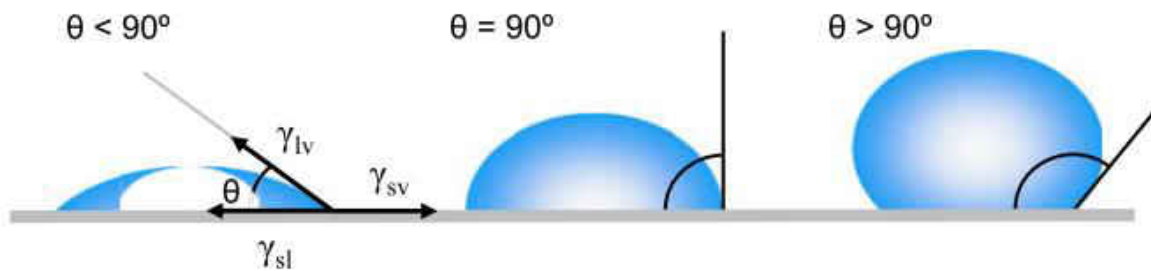
Figure 1: Schematic of droplet under wetting (left), partial wetting (center), and non-wetting (right) conditions

The surface tension forces of the solid-vapor, solid-liquid and liquid-vapor interfaces are denoted as γ_{sv}, γ_{sl}, and γ_{lv}, respectively. The relationship between these surface tensions and contact angle, described by Young[2], is,

$$\gamma_{lv} \cos \theta = \gamma_{sv} - \gamma_{sl} \qquad (1)$$

and can be seen in the left image of Fig. 1. These surface tensions can also be considered surface energies. In nature, all systems want to move toward states of least energy such a ball dropping, heat dissipating, and pressure induced fluid flowing. The interface of a fluid and solid substrate is no different in this regard. For a given system, when the surface energy of the solid-liquid interface is lower than the solid-vapor interface ($\gamma_{sl} < \gamma_{sv}$), wetting of the surface is said to be favorable, and the fluid will attempt to cover the solid[3]. By increasing the liquid-solid interface area and decreasing the solid-vapor interface area the surface energy of the solid decreases, resulting in a highly or partially wetting system ($\theta < 90°$) as seen on the left side of Fig. 1. In opposite cases where the surface is unfavorable ($\gamma_{sl} > \gamma_{sv}$), the liquid will attempt to cover as little of the substrate as possible resulting in a non-wetting system ($\theta \geq 90°$) as seen in the center and right side of the image in Fig. 1. In cases where the fluid being observed is water, substrates producing contact angles less than 90° are said to be hydrophilic and substrates producing contact angles of greater than 90° are said to be hydrophobic. Hydrophilic cases are covered moving forward as they are necessary for fluid dispersion on substrates.

Capillary Force

The phenomena responsible for the small amount of water climbing up the inside of a straw in a cup is known as capillary rise. This action is caused by the surface energy properties of the

water and the plastic straw. Assuming the straw-air interface has higher surface energy than the straw-water interface, the molecules around the triple line will tend to move upward to decrease the surface energy as seen in Fig 2.
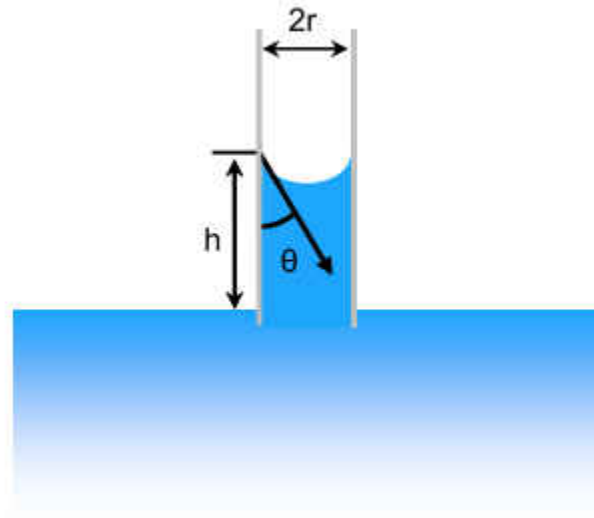
Figure 2: Example of capillary force pulling water into tube of radius, r, to height, h. Due to the wetting nature of the tube, a meniscus is formed with contact angle, θ.

These water molecules pull their neighboring water molecules along with them due to surface tension resulting in bulk fluid movement upward[3]. As the fluid moves upward in the straw, the weight of the fluid suspended becomes greater eventually resulting in a force balance between gravity and capillary force. This capillary force can be written as,

$$f = \gamma_{lv} p \cos \theta \qquad (2)$$

where γ_{lv} is the liquid-vapor surface tension, p is the contact line perimeter, and θ is the contact angle. In this case of the straw in water, the rise height h of the water inside the straw can be written as,

$$h = \frac{2\gamma_{lv}\cos\theta}{\Delta\rho g r} \qquad (3)$$

where $\Delta\rho$ is the difference in density between liquid and vapor, g is gravity, and r is the capillary radius (inner radius of the tube/straw). By decreasing the capillary radius, increases in rise height are obtained. There comes a point where the capillary radius is so small that capillary forces dominate over exterior forces such as gravity.

Micro-Capillary Dynamics

When a capillary with a very small radius ($r \ll 1$ cm) rise height characteristics are dominated by capillary forces. In a cylindrical micro capillary, capillary pressure, P_c, drives fluid upward. The velocity of the meniscus up the capillary can be written as,

$$V = \frac{r^2(P_c - P)}{8\eta l} \qquad (4)$$

where r is the capillary radius, P is the gas pressure in the capillary, η is the dynamic viscosity of the fluid, and l is the length of the water column[4]. For an open capillary, gas pressure, $P = const < P_C$, shows that the velocity will decay over time but always be greater than 0. This is the case for non-evaporating capillary motion as the surface area of the fluid exposed to air is extremely small ($\frac{A_{lv}}{A_{ls}} \approx 0$). This is important as we move forward into sections where similar phenomena arise but exposed surface areas are vastly different.

Surface Roughness and Wetting

With the increases in micro-/nano- structuring technology, high-precision structuring of substrates has become more widely used to study spreading, wicking, zippering, and building of

thin films. Nanopillar arrays have been amongst the newest additions to the scientific realm of thin film studies. Propagation velocity, wicking distance, and wicking force of thin films on hydrophilic substrates have been the focus of many scientific articles since the introduction of the micro-/nano-structuring of substrates. These studies are pioneering a new method for increasing the distance of two phased flow conditions needed in heat pipes before single phase, superheated vapor is achieved.

Hemi-Wicking

In the investigation of textured substrates and their effect on apparent contact angle (θ^*), the conclusion made by Shibuichi et al.[5] from the Kao Corporation stated that texturizing the surface of a substrate can modify the apparent contact angle of the film as seen in Fig. 3.
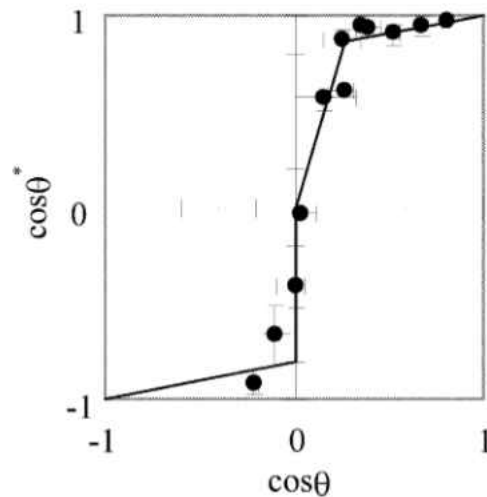
Figure 3: Apparent contact angle vs. Contact angle

Observing the difference of the liquid traversing the textured substrates in hydrophobic and hydrophilic cases, Bico et al.[6] appropriated the phrase "hemiwicking". This term was used to

describe the cases where a hydrophilic, texturized substrate was to be wetted by a liquid film in which the liquid film has an intermediate step between spreading and imbibition ($\theta = 0$ and $\theta < \pi/2$, respectively). The ability of a textured surface with roughness (r) and fraction of solid/liquid interface (φ_s) to drive a liquid was then found to be directly manipulatable. The studies focused on the wetting and contact angle of a drop or film deposited above the textured substrate[6], [7]. By using the Wenzel's relation,

$$\cos \theta^* = r \cos \theta \qquad (5)$$

Bico et al. looked at the contact angle and found that drops will have an apparent contact angle (θ^*) less than that of the contact angle of the same liquid on a smooth substrate of the same material (θ) when $r > 1$ and $\theta < \pi/2$. Hemiwicking is then said to occur if the change in interfacial energy as a function of x (dF/dx) is negative. A criterion was then constructed[6] saying the contact angle (θ) will be less than the critical contact angle (θ_c) when

$$\theta_c = \cos^{-1}\left(\frac{1-\varphi_s}{r-\varphi_s}\right) \qquad (6)$$

It can be see that as $r \rightarrow \infty$, $\theta_c = \pi/2$ which is the classical condition for capillary rise. As such a critical angle can be described $(0 < \theta_c < \pi/2)$, there are two cases for observed contact angle; $\theta_c < \theta < \pi/2$ and $0 < \theta < \theta_c$. When the contact angle is greater than that of the critical contact angle ($\theta > \theta_c$), the solid will remain dry beyond the drop. However, when the contact angle is less than that of the critical contact angle ($\theta < \theta_c$), the fluid will penetrate outward into the textured substrate and the drop will sit upon a mixture of solid and liquid with apparent contact angle of θ^* (Fig. 4). This case ($\theta < \theta_c$) became the focus of many more studies[8] analyzing the dynamics of this hemiwicking process.
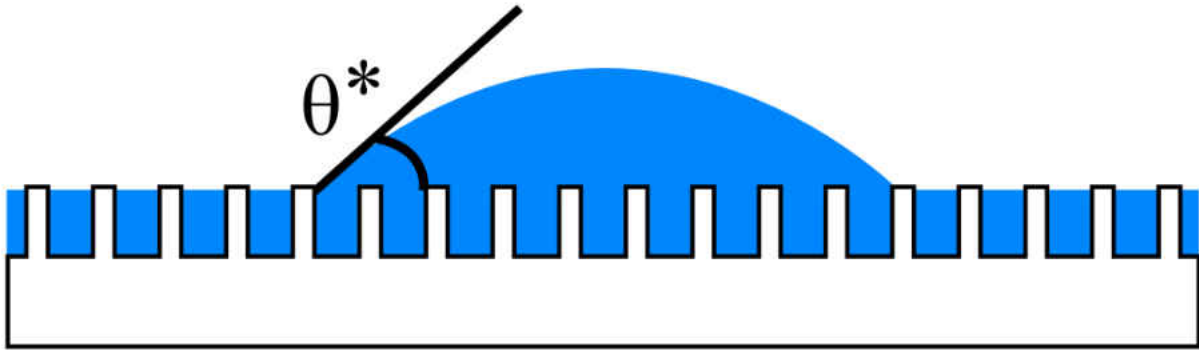
Figure 4: Fluid Penetration into rough surface with apparent contact angle

<u>Driving and Resistive Forces</u>

Capillary forces and viscous forces drive the wicking phenomena. Viscous forces between the fluid and substrate restrain the fluid and capillary forces encourage the fluid to penetrate the porous substrate. As said before, the substrates under investigation are hydrophilic with roughness determined by wicking pillar height and solid/liquid interface by pillar spacing and diameter (Fig. 5).
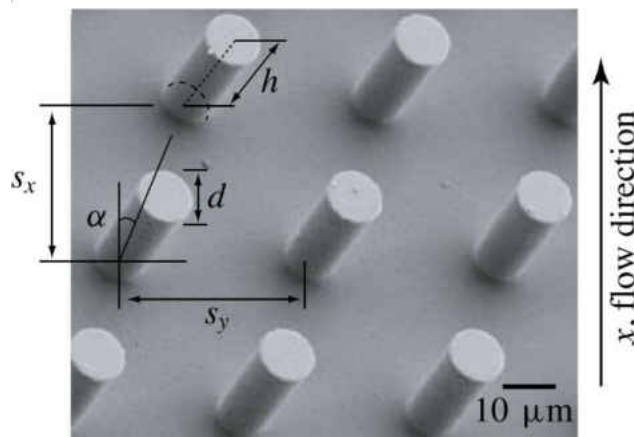
**Figure 5: Example of micro pillar array on substrate with size, spacing, and orientation**

The penetration process is the movement of the interface in the porous material that is advancing or seen to be in advance of the bulk fluid layer. As fluid moves through the micro structured substrate the fluid will wick up the pillars from the base to the height of the pillar (h). This upward motion is caused by a surface energy difference between the solid-liquid interface and solid-vapor interface. The criteria for upward wicking is when the surface energy (tension) of the solid-liquid interface is less than that of the solid vapor interface ($\gamma_{sl} < \gamma_{sv}$) [9]. If this criterion is met, the fluid will continue to propagate up the wick until either the fluid reaches the top of the wick or the fluid reaches equilibrium with surface tension and viscous forces. In a case where a substrate is completely covered in these micro pillar arrays, the fluid will move through the array with driving force of *F = γ(r-1)*, where $\gamma = \gamma_{lv}$ and r is roughness (r > 1). The roughness factor can be effected by the placement and size of the pillars in the array. By denoting the radius, height, and pitch of the pillars as b, h, and p respectively, the roughness can be described by the relation: *r = 1 + 2πbh/p²*. Driving force can then be deduced to:

$$F_D = \frac{2\gamma\pi bh}{p^2} \qquad\qquad (7)$$

The fraction of solid/liquid interface (φ_s) as reviewed earlier can be written as $\varphi_s = \pi b^2/p^2$ for pillar array cases. The resisting force friction can be calculated and then used to calculate dynamic coefficient (D). This dynamic coefficient is used by Washburn's law which states the film front propagates as the square root of time *(z ~ (Dt)¹ᐟ²)* where D is dependent on the liquid properties and tube radius (D ~ γb/η) [9]. The study[8] went further into this hemiwicking process creating scaling laws for film front propagation velocity, wicking force, and resisting force by changing the roughness (pillar heights, spacing, and pitch) of the hydrophilic substrate. The use of deep reactive ion etching processes have resulted in extremely detailed arrays of micro structured pillars with

radii of 10 μm and various spacing configurations. After manufacturing these substrates, measurements of fluid front motion through the pillar array ($\dot{L}$) were recorded for several roughness specifications. Not only were measurements and theorizations made for $\dot{L}$, but also calculations of the 2-D fluid velocity (U(y,z)) through the pillared array behind the liquid front were implemented.
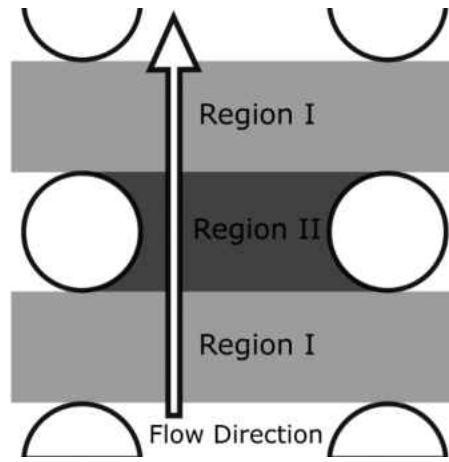
Figure 6: Schematic of region 1 and 11 for velocity profile calculations

By breaking the fluid flow region into two separate cases, u(y, z) and u'(y, z), where u and u' were velocity in region I (before encountering pillars) and velocity in region II (between pillars) (Fig. 6). It was found that that for regions I and II the velocity surface plot could be calculated using

$$u(y,z) = U_m\left(2\frac{z}{h} - \frac{z^2}{h}\right) \qquad (8)$$

$$u'(y,z) = U'_m\left(2\frac{z}{h} - \frac{z^2}{h}\right)\left(1 - 4\frac{y^2}{s_w}\right) \qquad (9)$$

respectively, where U_m is maximum velocity in region, h is the height of the pillars, and s_w ($\bar{s}$) is the average wall to wall spacing of pillars throughout region II. These 2-D velocity profiles were then used to calculate flowrates in regions I and II that very nicely result in $q_1 = \frac{2}{3}U_m s_y h$ and

14

$q_1 = \frac{4}{9} U'_m \bar{s} h$ repectively. These flow rates were used to get average fluid velocity values (U, U')

for regions I and II. Shear forces from the unimpeded flow (region I) as well as the shear forces

for the base and sides of the impeded flow (region II) were calculated (F_1, $F_{2,B}$, and $F_{2,S}$). The total

force acting on a unit cell with dimensions s_y (spacing normal to flow) and s_x (spacing along flow

direction) was scaled using,

$$\hat{F}_r = F_1 + F_{2,B} + F_{2,S} \qquad (10)$$

When simplified, the scale of the resisting force per unit width on a film of L propagation distance

away from the source is found to be

$$F_r = \frac{L}{s_x s_y} \hat{F}_r \sim \mu U L \left(\frac{1}{h} + \frac{f-1}{s} \right) \qquad (11)$$

Where f is roughness (f ≡ r) and is found using $f = 1 + \frac{\pi d h}{s_x s_y}$, and μ fluid viscosity. Then with the

use of relation for driving force, $F_d \sim \frac{\pi \gamma d h}{s_x s_y}$, and using the previous definition of f, driving force

becomes

$$F_d \sim (f - 1)\gamma \qquad (12)$$

which is consistent with Ishino et al.[9]. Balancing these two forces yields the scaling law of the

microscopic distance and velocity,

$$L \sim \left(\frac{\gamma \eta h}{\mu} \right)^{1/2} \sqrt{t} \qquad (13)$$

$$\dot{L} \sim \frac{\gamma}{\mu} \frac{\eta h}{L} \qquad (14)$$

respectively, where η is a dimensionless structural coefficient that is solely specified by the

dimensions of the pillar array: $\eta = \frac{f-1}{1 + \frac{h(f-1)}{s}}$. When L was plotted vs the square root of time and

pillar width ($s = s_y - d$) (L vs. $t^{1/2}s^{1/2}$) for several cases of pillar spacing and pitch, it showed that L increased linearly with $\sqrt{t}$ but with varying slopes. When the L was plotted with the scaling law ($L \sim \left(\frac{\gamma \eta h}{\mu}\right)^{1/2} \sqrt{t}$) and then scaled with the capillary length, $l_c = \left[\frac{\gamma}{\rho g}\right]^{1/2}$, these lines all collapse down to one straight line, validating the theory made by Kim et al [8].

Liquid Meniscus

Curvature of the meniscus is one of the most important characteristics of the film profile as this controls, indirectly, the evaporation rate. The evaporation process is the most important function of a thin film used in micro electronic device cooling as it activates the latent heat of the fluid allowing for very high heat transport rates. In a film extending from height (h >> 1 µm), there are three regions; a bulk/intrinsic region where capillary forces dominate, a thin-film region where long-range molecular forces are felt, and a non-evaporating region where the liquid is adsorbed on the substrate (Fig. 7).
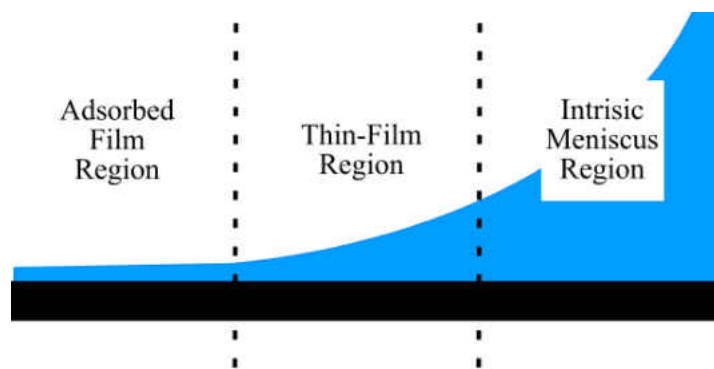
Figure 7: Schematic of Meniscus detailing adsorbed film, thin-film, and intrinsic meniscus (bulk fluid) region. The region of interest, and of highest evaporative mass flux and heat transfer, is the thin-film region. This region of the meniscus is defined as the region supported by disjoining pressure and

is measured from contact line of the adsorbed film (pseudo-triple line) to the location where the film is approximately one micron thick (where capillary forces begin to dominate) [10]. As the length of this region is purely based on the gradient of the thickness profile, high interfacial curvatures lead to higher heat flux for a defined fluid.

<div align="center">Meniscus Extension from Wicking Structures</div>

For cases where there are extending meniscus, the liquid wet front location on the base relative to the pillar of which the liquid has reached the top is denoted by x_0. If the distance to the next row of pillars is shorter than this distance, the liquid will begin to climb the next hydrophilic pillar. If the pillars cease to exist after row n, the meniscus will extend out to a distance x_0. To calculate x_0, we must consider the meniscus hanging on the pillars at the wet front. The capillary force along the pillar perimeter $F_c = \pi d \gamma$ is balanced with by the force due to the pressure drop (Δp) across the interface of the meniscus covering the area $s_y x_0$. This pressure drop gives $\Delta p \approx \frac{\pi d \gamma}{s_y x_0}$ which can be related to the meniscus curvature via the Young- Laplace equation,

$$\Delta p \approx \gamma \frac{\partial^2 z}{\partial x^2} \sim \frac{\gamma h}{x_0^2} \qquad (15)$$

which, when equated, yields $x_0 \sim \frac{h s_y}{\pi d}$ [8]. This is very interesting because the meniscus in the case is extending out normal from row n of pillars, making the profile quasi-two dimensional, where the meniscus volume per longitudinal pillar spacing (s_y) can be solved with integration of the profile over x_0:

$$V_m = s_y \int_0^{x_0} \delta(x) dx \qquad (16)$$

which will be used later in the study.

Meniscus Curvature

Curvature of the thin film meniscus region is maybe the most important characteristic of a film as curvature is directly related to evaporation. By increasing the curvature of the thin film region, higher evaporation rates and heat transfer coefficients can be achieved. With a known thickness profile of the thin film meniscus region, the curvature of the film, K, can be calculated using the following equation,

$$K = \frac{\frac{d^2\delta}{dx^2}}{\left(1+\left(\frac{d\delta}{dx}\right)^2\right)^{3/2}} \qquad (17)$$

where δ is film thickness and x is displacement from the contact line [11]. This curvature is a result in surface tension gradients along the surface of the film resulting in a un equal force balance causing flow to move toward the triple line. The tendency of flow to move toward the triple line is called the Marangoni effect and be seen in everyday life [12], [13]. This effect if responsible for coffee rings, rings on a wine glass that has been left out and allowed to partially evaporate.

Hydrogels

A hydrophilic polymer network that is swollen with water is called a hydrogel or colloid gel [14]. In general, the term 'gel' indicates that over 50% of the total mass of the hydrated film is water. The dehydrated (dry) film is considered to be a solid on a macroscopic level, having definite shape and not able to flow, but on the microscopic scale it behaves as a solution, allowing water soluble molecules to diffuse into the hydrogel[15]. Due to their lack of mechanical strength[16]–

18

[18], the application of these hydrogels as a mechanical device are limited and therefore are primarily used in the medical field but have also been used in disposable diapers for their strong liquid absorptivity. Studies of these hydrogels and their effects on capillary force, contact line dynamics, and heat transfer are on the forefront of the newest efforts on utilizing them for mechanical uses. When a thin layer of hydrogel, poly(N-isopropylacrylamide) (PNIPAM), was applied to the inside of a tube like in Figure 2 and the filling time of the tube was recorded to be three orders of magnitude larger than an uncoated tube (Fig 8) [19].
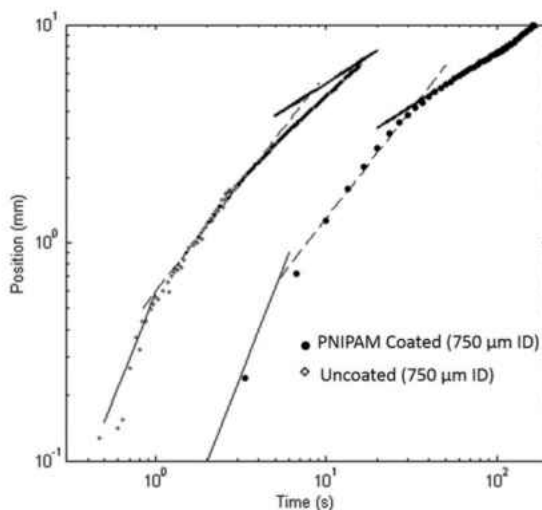
Figure 8: Meniscus position vs. time for glycerol in a bare, uncoated glass capillary with 750 mm ID (open diamonds) and PNIPAM coated glass capillary with 750 mm ID (filled circles). The thin lines are lines of slope 2 (corresponding to inertial filling behavior), the dashed lines have slope 1 (corresponding to the convective loss regime), and the thick lines have slope 1/2 (corresponding to the Washburn regime). The shift to longer times is due to higher contact angle for glycerol on PNIPAM than on glass [19]

However, they present a more complex problem along the contact line. These films act almost as the wicking structures with contact angle less than critical contact angle (fluid extending outward from the droplet. The fluid imbibes the hydrogel and penetrates outward from the film. As the fluid completely saturates the hydrogel film, the film swells. The dry and hydrated thickness of

19

the coatings were measured in this study [19] and curve fit line was used to predict the values of

fully hydrated film thickness using varying initially dry film thickness (Fig 9).
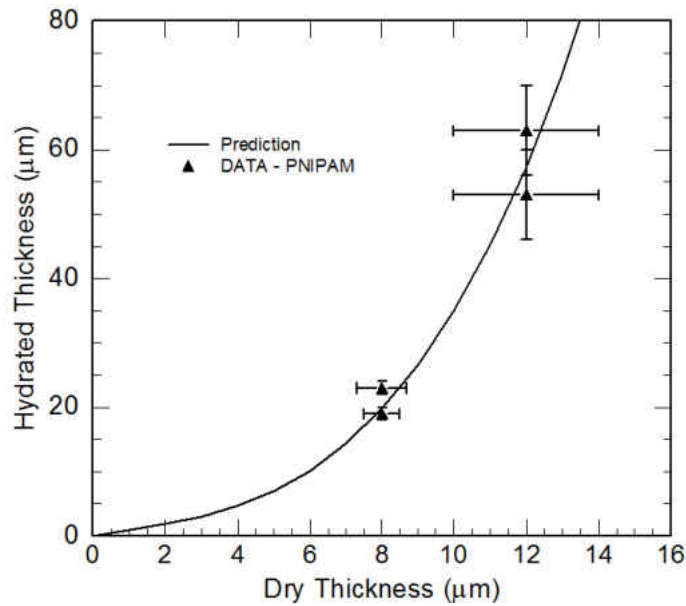
Figure 9: Relationship between dry and hydrated hydrogel (PNIPAM) coatings. Results taken from tabulated results of measured thicknesses of four samples with PNIPAM hydrogel coatings. A polynomial curve fit was used to predict the nature of swelling ratios.

The intermediate step and section of film between the completely dry hydrogel film and fully

hydrated film is designated as the partially hydrated film, resulting in a gradient in film thickness

[19], [20] (Fig 10).
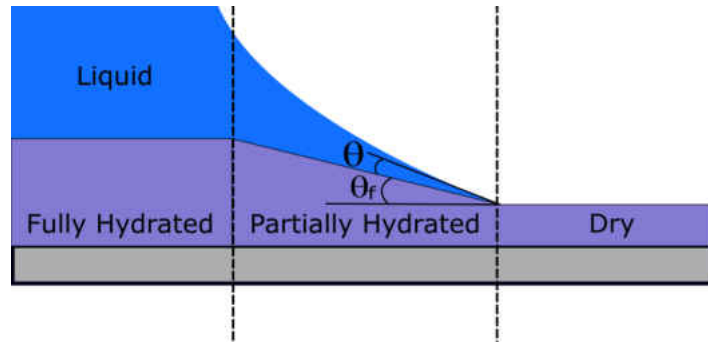
Figure 10: Schematic of meniscus on hydrogel. Three section of the hydrogel can be observed and labeled as Fully hydrated, partially hydrated, and dry region. This transition creates a gradient in thickness with angle θ_f effecting contact angle, θ.

This phenomenon is responsible for very complex contact angle and line dynamics. These contact line dynamics are strongly influenced by the rheology of the gel [21]. Generally, hydrophilic hydrogels promote contact line motion in the form of a series of stick-slip actions (Fig. 11) [19]–[21], and in cases of high velocity and very low velocity movement it can be seen to move continuously [20], [21].
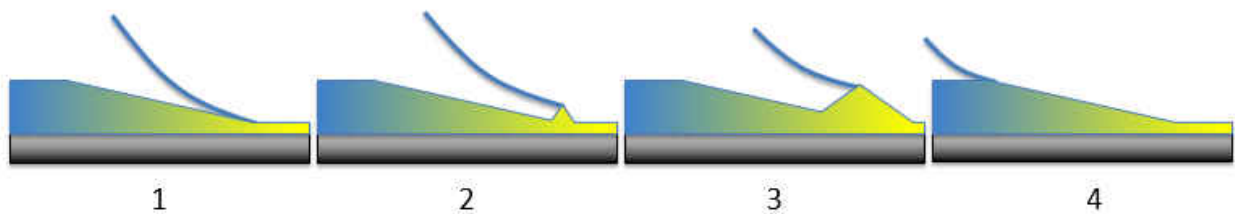
Figure 11: Hydrogel Wetting and spreading dynamics. Liquid builds meniscus on partially hydrated hydrogel (1), a pressure point is made and the hydrogel begins to swell at the contact point (2), fluid continues to imbibe hydrogel and produces swelling (3), full hydration is achieved at pinned contact line (4), fluid then wets down the surface and re-pins (1).

For cases where the contact line movement is slow so that the rate of swelling approaches the rate of motion, meaning $\theta_f \rightarrow \theta$ (Fig 10 (right)), the contact line motion will cease and reverse upon

the condition of $\theta_f = \theta$ [20]. At this point, the fluid will continue imbibing the fluid thus decreasing the hydrogel swelling angle and resuming the stick slip conditions. The rate of imbibition, $\dot{m}_{imb}$, will slow down as the fluid approaches steady state until complete film hydration is obtained or evaporative mass flow, $\dot{m}_{evap}$, reaches the fluid feed rate, $\dot{m}_{syr}$, as seen by,

$$\dot{m}_{syr} = \rho_f \frac{dV_m}{dt} + \dot{m}_{evap} + \dot{m}_{imb} = 0 \qquad (18)$$

where ρ_f is the density of the fluid, and V_m is the volume of the meniscus.

CHAPTER 3: EXPERIEMENTAL SET UP AND PROCEDURE

A combination of reflectometer and optical interferometer allow film thickness and curvature measurements of the thin-film meniscus. A series of mirrors and lenses allow both systems to make simultaneous measurement of the film characteristics (Fig. 12) at any location. The assembly responsible for producing a uniform, repeatable meniscus was designed and manufactured in house at the University of Central Florida (UCF). The samples used in this experiment, were purchased through GM Associates Inc. and the depositions of titanium, silicon dioxide (SiO_2), and hydrogel were then implemented.
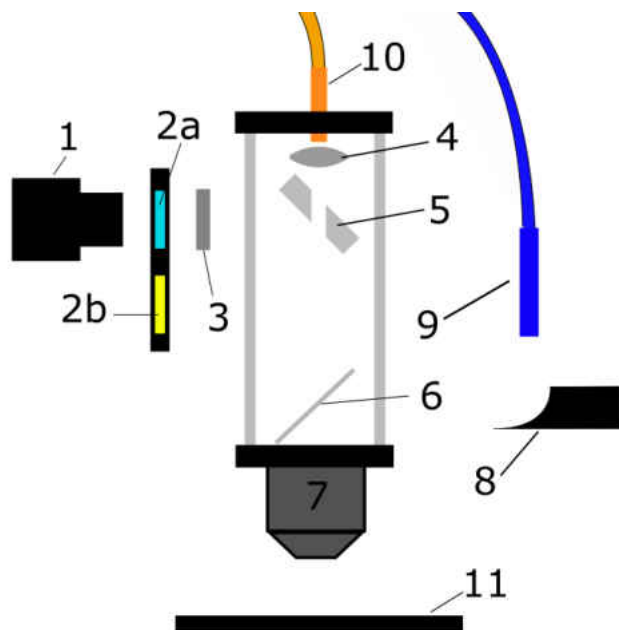
Figure 12: Schematic of Spectrometer/Optical Interferometer setup. Components include; (1) camera, (2a) 656 nm bandpass filter, (2b) 450 nm bandpass filter, (3) achromat [f = 120mm], (4) planoconvex lens [f =20mm], (5) pinhole Ag mirror, (6) 50-50 beam splitter [th=1mm], (7) 15x reflective objective, (8) off-axis parabolic mirror [f_2=15mm], (9) optical fiber from light source, (10) optical fiber to spectrometer, (11) substrate.
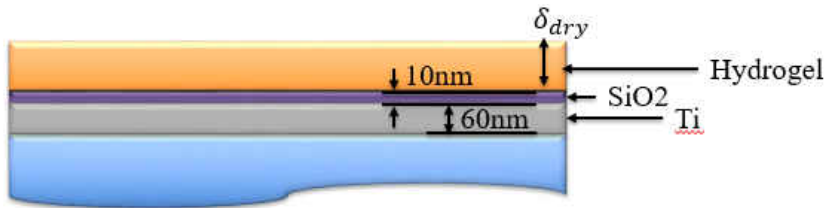
Samples

Titanium and SiO$_2$ were deposited in house at UCF's Center for Research and Education in Optics and Lasers (CREOL) using evaporative metal deposition and Plasma Enhanced Chemical Vapor Deposition (PECVD), respectively. The nominal thickness of deposited titanium was 60 ± 10 nm and was verified using time domain thermo-reflectance (TDTR). The thickness of SiO$_2$ was measured by reflectometry.

The hydrogel thicknesses being deposited range for 30 nm to 1 μm and were deposited by Ali Kosar and his team at Sabanci University in Istanbul, Turkey. The minimum value of 30 nm was chosen to measure the effect of a hydrogel coating with thickness less than that of the adsorbed film [22]. The maximum thickness of 1 μm, relating to the approximate maximum thickness of the thin film region. The incremental dry hydrogel thicknesses of Sample 1-5, beginning with minimum thickness and ending with maximum thickness as discussed, are 100 μm, 250 μm, and 500 μm. For a control sample, to measure the curvature characteristics of a film before the implementation of a hydrogel coating, a sample was made with only titanium and SiO$_2$. The final product for said samples can been seen in Fig. 13 and Table 1.

Table 1: Deposition thicknesses for sample 1-6.

| Sample	Titanium Thickness (nm)	SiO$_2$ Thickness (nm)	Hydrogel thickness (nm)
1	57.1	10	500
2	65.3	20	30
3	61.8	20	100
4	55.75	5	250
5	63.3	10	1000
6	65.4	10	0

Figure 13: Schematic for substrate layer profile. Materials deposited on Fused Silica for samples 1-5 include Titanium [Ti], Silicon Dioxide [SiO₂], and Hydrogel.

Liquid Film Rig

To build a reliable, uniform liquid meniscus on a substrate, the substrate must be held steady, level, and clean. These were the criteria used in designing and manufacturing the setup that would be responsible for building consistent liquid films on test samples. The structure, inside which the fluid is pumped, is made of Teflon due to its low surface energy (non-wetting nature) and chemical resistivity. A Viton O-ring of high chemical resistivity, is used on the inside of this structure to ensure a correct and complete seal. The fluid builds radially inward and therefore the O-ring is on the inside wall of the Teflon structure and support materials can be implemented on the outside of the structure. When pressing the Teflon structure down to achieve O-ring sealing, the load must be uniform to ensure minimal local deflection. An aluminum load distributor was manufactured to provide the necessary pressure to force a proper seal. Any leaks in the system will render the evaporation rates useless as the evaporation rate is measured according to pump feed rate. At steady state conditions, the feed rate is equal to the evaporation rate as the film volume is held constant. The fluid is fed into the structure using a stepper motor driven syringe pump controlled by LabVIEW. The whole assembly (Fig. 14), with substrate, is bolted to a support plate. This support plate can be moved in two dimensions by X and Y axis stepper motors that are also controlled in LabVIEW.
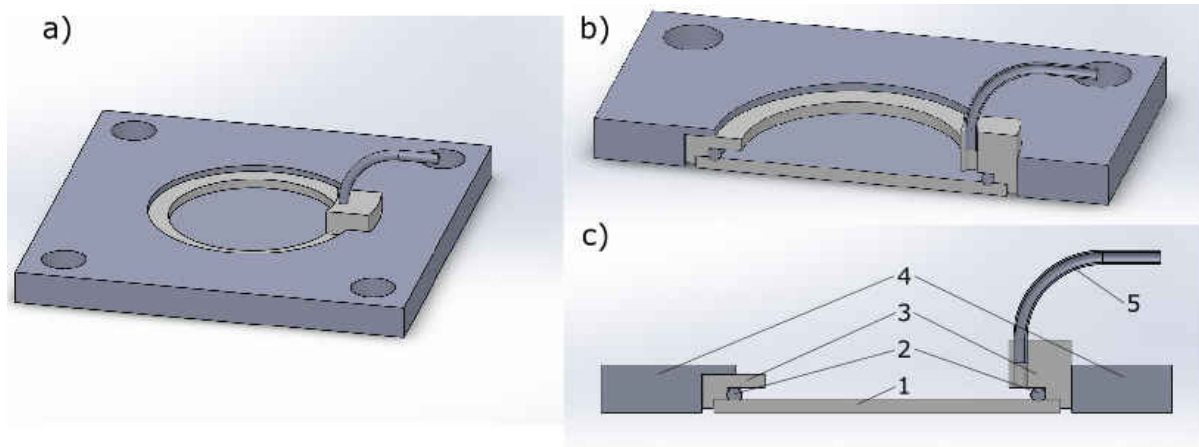
Figure 14: Drawing of meniscus building structure fed by LabVIEW controlled syringe. a) complete 3-D view of full assembly, b) Cross sectional 3-D view, c) isometric view of components including substrate (1), O-ring (2), Teflon structure (3), load distributor (4), and syringe (5).

Spectrometer

The implementation of a spectrometer allows for reflectance measurements of the films. By using a variety of light sources ranging ultraviolet (UV), visible light (VIS), and infrared (IR), it was possible to get high fidelity measurements of reflectivity of films under investigation. Four light sources were used including deuterium, halogen, a cold white diode, and an infrared diode. The wavelengths and intensity of light sources can be seen in Fig. 15, respectively.

26
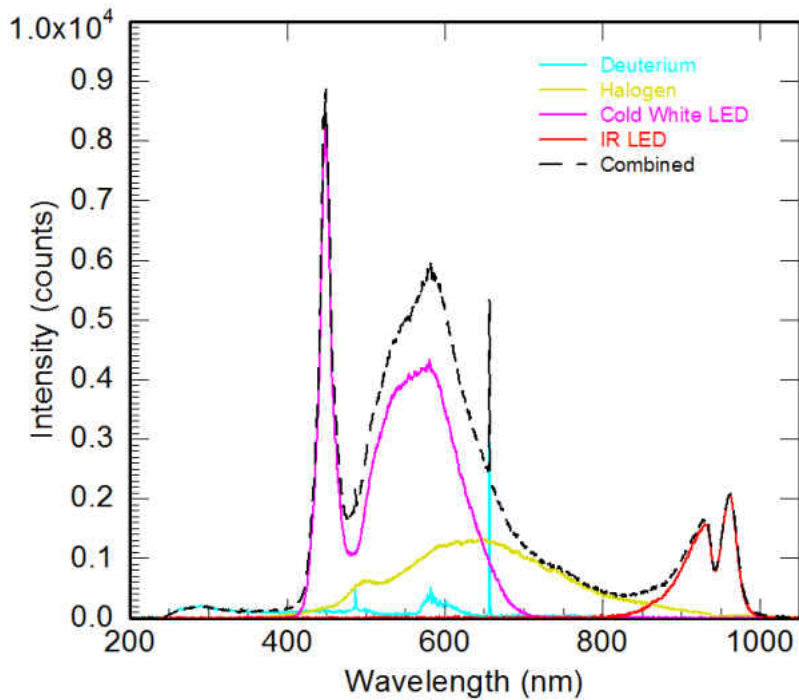
Figure 15: Light source intensity distribution per light source with total. Deuterium (blue) ranges from 100 nm to 800 nm, halogen (yellow) ranges from 300 nm to 1100 nm, cold white LED (MCWHD3) (pink) ranges from 400 nm to 750 nm, and the IR LED (TL-M940D2) (red) ranging from 800 nm to 1000 nm, giving a complete light source range (black-dashed) of 190 nm to 1100 nm. Signal was calibrated using Si.

These lights are not directly applied to the substrates and films as they are reflected and focused through several optical components in the setup as seen in Figure 12. Due to imperfect reflection, transmission, and absorption of mirrors and optics, loss of intensity of light though the setup is guaranteed. To accurately calculate the intensity of the light being emitted to the substrate, a series of calibrations were conducted using silicon (Si), silicon dioxide (SiO$_2$), gold (Au), and germanium (Ge) mirrors.
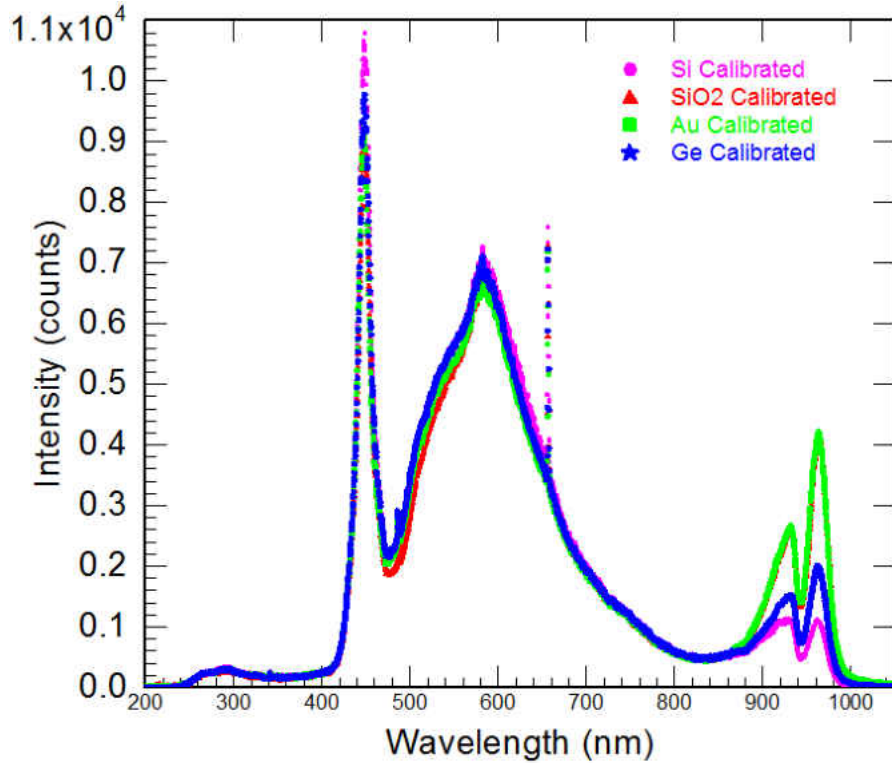
Figure 16: Light source (I₀) calibration by sample; silicon (pink circle), silicon dioxide (red triangle), gold (green square), and germanium (blue star).

The calibration of the Light source intensity, $I_0(\lambda)$, was measured and calculated from spectrometer readings and well know reflectance literature data of the four different substances (Fig. 16) using;

$$I_0(\lambda) = \frac{I_i(\lambda)}{R_i(\lambda)}$$
(19)

where $I_i(\lambda)$ is the measured intensity spectrum for each substance (i = Si, SiO₂, Au, Ge) over wavelength range λ = [200, 1050] nm, and $R_i(\lambda)$ is the literature reflection data using a numerical method incorporated with a variety of data bases by Fredrik Hansteen. The results were used to compare calculated reflectance using the calibrated light source spectrum to the literature reflectance data from each of the calibration substances as:

$$R_i(\lambda) = \frac{I_i(\lambda)}{[I_0(\lambda)]_j} \quad \text{for cases i} \neq \text{j} \qquad (\ 20\ )$$

where $[I_0(\lambda)]_j$ is the calculated light source intensity for substance, j. To correctly display that the

spectrometer has been calibrated, reflectance measurements of each substance using the light

source intensity spectrum calibrated from other materials can be shown. For example, by observing

the measured reflectance of silicon dioxide using the light source intensity spectrum calculated

using Germanium, and comparing the result with literature reflectance data for silicon dioxide, an

idea of how accurate the germanium reflection data, SiO_2 reflectance data, and spectrometer data

can be obtained. The results confirm the accuracy of all data and spectrometer readings (Fig. 17).
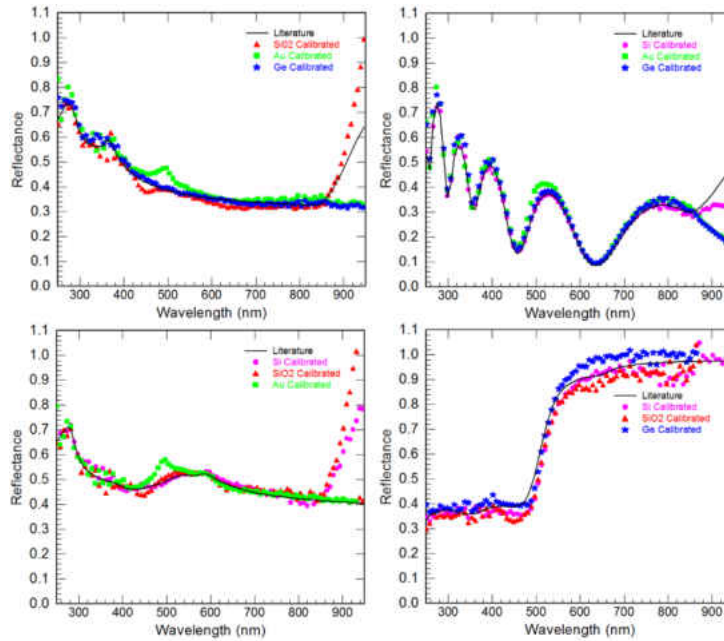
**Figure 17: Reflectance measurements using calibration samples for comparison with literature data. (Top Left) Si measured using calibrated light source from SiO_2, Au, and Ge, (Top Right) silicon dioxide measured using calibrated light source from Si, Au, and Ge, (Bottom Left) Ge measured using calibrated light source from Si, SiO_2, and Au, (Bottom Right) Au measured using calibrated light source from Si, SiO_2, and Ge.**

<u>Reflectometer</u>

When measuring films with thicknesses on the order of nanometers, typical measuring devices such as calipers and rulers are of no use. To measure the thickness of these ultrathin films, light and its reflectance are measured and analyzed. The thickness of the film is then fit to literature values and numerical methods using a variety of databases.

After calibrating the spectrometer to acquire the light source intensity, the focus was moved to being able to calculate thin film thicknesses. These films must be constant in thickness for the reflectometer to work. A sample of SiO_2 on Si was used to measure and predict the value of the SiO_2 thickness. It was seen that the thickness of the SiO_2 layer was 545 nm by comparing the result to that of a numerical model (Fig. 18).
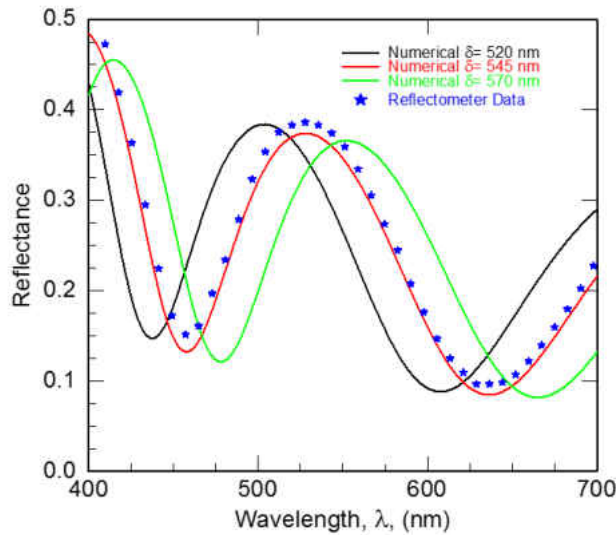
Figure 18: Reflectance data for a thin film of SiO_2 compared with literature data for films of thickness 520 nm, 545, nm, and 570 nm.

To calculate thickness profiles of non-uniform films on a substrate, a slightly different method of reflectometry, called interferometry, is used. This method involves observing monochromatic light passing through a film at multiple areas and measuring the intensity as a function of displacement, $I_\lambda(x)$. The oscillatory nature of the light intensity and the spacing of peaks and troughs (light and dark bands) give an accurate calculation of the angle of the fluid-vapor interface, θ. By calculating this angle across a given displacement, $\theta(x)$, a film profile can be achieved. The equation used in this experiment to calculate the thickness profile of a film is,

$$\delta_{i+1} = \delta_i + \tan\theta_i \, dx$$

For this setup, two different wavelengths of light can be used to measure thickness profiles, 450 nm and 656 nm light, corresponding to the bandpass filters used (2a and 2b in Figure 12). For a film of constant thickness profile slope (linear increase), the theta can be observed as uniform. Films of exponentially increasing thickness will have linear or exponentially increasing theta terms. A calibration of the set up was conducted using three cylindrical lenses and a measurement of the vapor meniscus was made. The results can be seen in Figure 19.
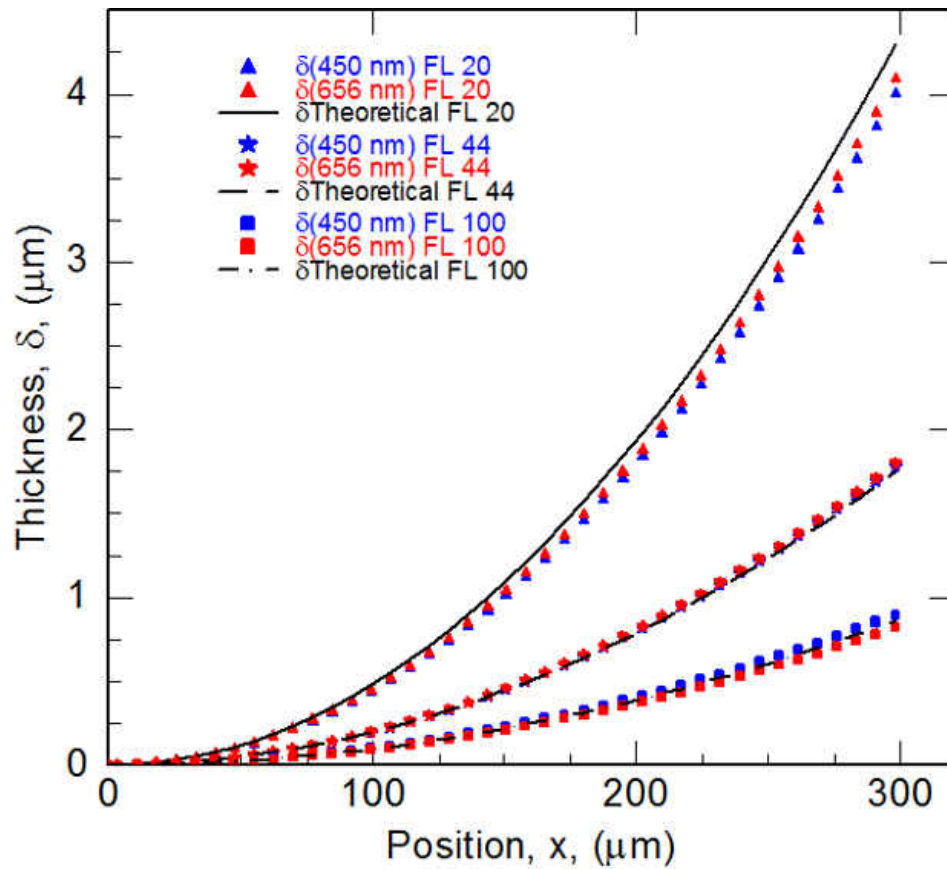
**Figure 19: Calibration measurements of films created by cylindrical lenses with focal lengths (FL) of 20 mm, 44 mm, and 100 mm on a substrate using 450 nm and 656 nm light.**

From the calibration results, the interferometer can be said to be accurate and reliable. The curve fit of the interferometer can achieve profile calculations using polynomial curve fitting for fringe frequency, f, up to 5th order polynomials.

CHAPTER 4: RESULTS AND DISCUSSIONS

Film Measurements and Analysis

To correctly measure the thickness profile of liquid films, many variables must be known and considered. First, the structure of these films must be known and each must be able to be measured. As previously discussed, the film has three distinct sections, the adsorbed film, the thin film region, and the bulk fluid region. The adsorbed film is uniform in thickness and, therefore, will be measured using the reflectometer. This will give us the starting thickness for the zeroth fringe thickness (δ_0) which is incorporated into the interferometer measurements as the film starting thickness. The thin film region and bulk fluid region are varying in height and will be measured using the interferometer (Fig 20).
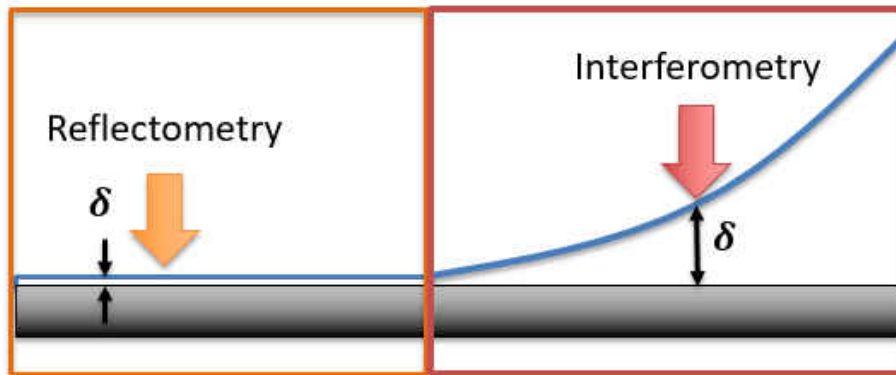
Figure 20: Schematic of thin film and measurement technique used. Reflectometry was used to measure the adsorbed film of constant thickness to obtain zeroth fringe, δ_0, which is used as the starting point for the thin film region using interferometry.

The maximum height of the bulk region is 1 mm, constrained by the clearance between the substrate and the Teflon structure. This constraint will be used when viewing the film in the vicinity near the structure as the structure disrupts the light from the camera distorting the image.

Steady state conditions are difficult to achieve in real life situations. Before tests can be done with hydrogels, the steady state assumption for this experiment must be proven to be possible. Water on SiO_2 is observed over the span of several hours to determine the capability of this rig to produce films considered to be at steady state. The meniscus was first built by pumping fluid at 1000 nL/s until a symmetrical film was made around the inner annulus of the structure with x_o=5mm. The flow rate was then turned to 25 nL/s and the meniscus was allowed to evaporate freely. After three hours, the meniscus was observed to be constant and measurements were then conducted every 90 minutes for three hours. Measurements were taken at times; $T_1 = 0$, $T_2 = 90$ minutes, and finally $T_3 = 180$ minutes. Water was pumped into the meniscus at 25 nL/s ($\dot{m}_{syr} = \dot{m}_{evap} = 25 \, nL/s$) and the room temperature was measured to have a nominal value $T_{amb} = 21 \pm 2°C$. The results of the experiment can be seen below in Figures 21-23.

Figure 21: Measurement of meniscus profile at time t = 0 (Fluid is H$_2$O, T$_{amb}$ = 21°C). Meniscus was measured using interferometry with two separate wavelengths of light (blue triangle denotes 450nm, red triangle denotes 656nm) and the average of the two measurments have been added (black line).
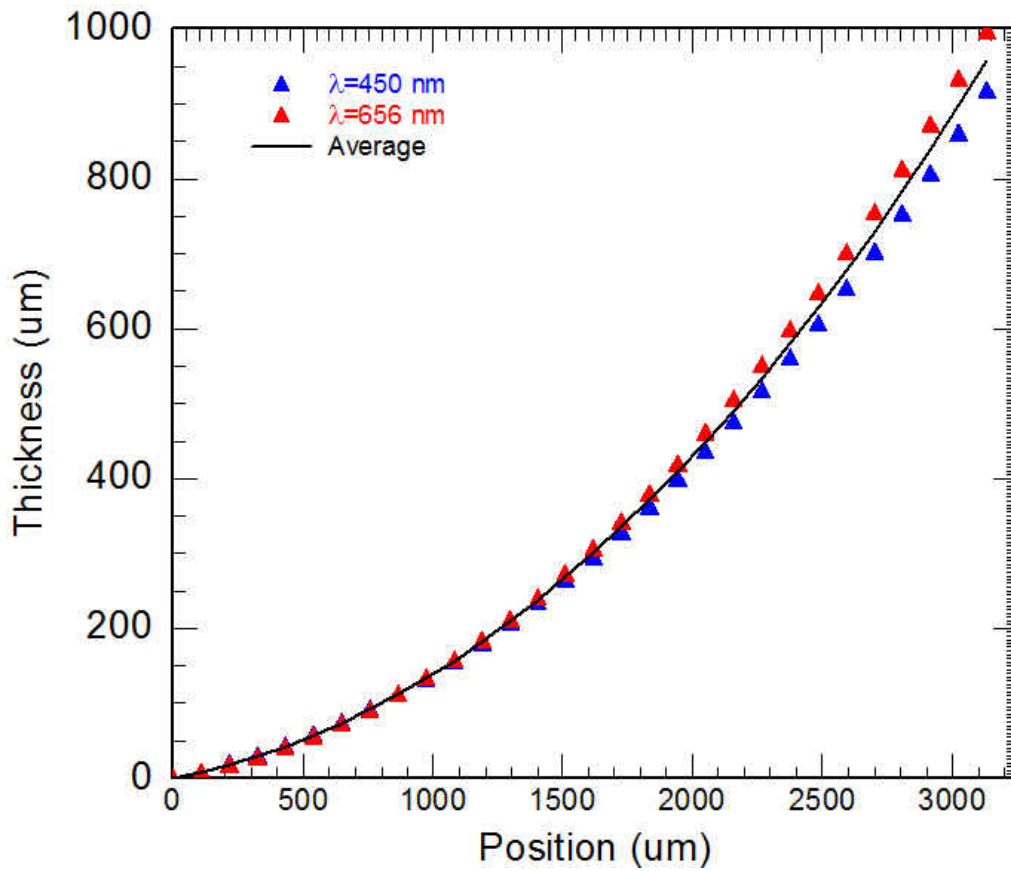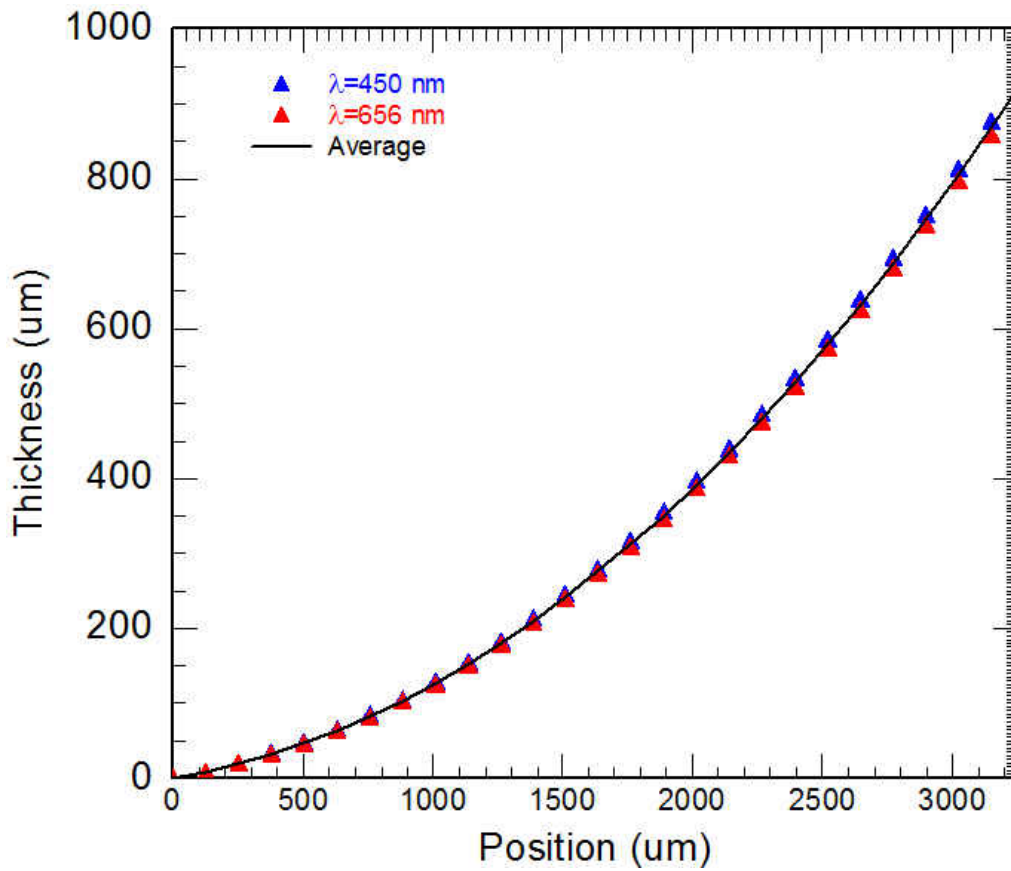
Figure 22: Measurement of meniscus profile at time t = 90 min (Fluid is H_2O, T_{amb} = 19°C). Meniscus was measured using interferometry with two separate wavelengths of light (blue triangle denotes 450nm, red triangle denotes 656nm) and the average of the two measurments have been added (black line).

Figure 23: Measurement of meniscus profile at time t = 180 min (Fluid is H₂O, T$_{amb}$ = 21°C). Meniscus was measured using interferometry with two separate wavelengths of light (blue triangle denotes 450nm, red triangle denotes 656nm) and the average of the two measurments have been added (black line).
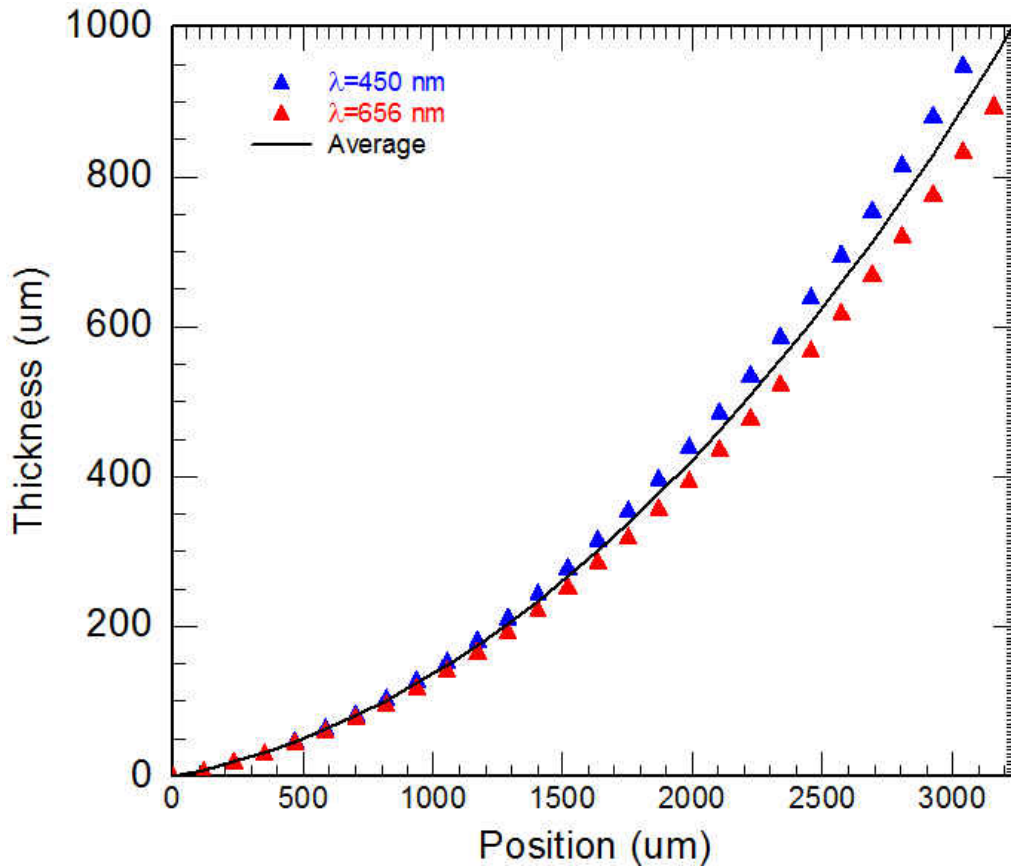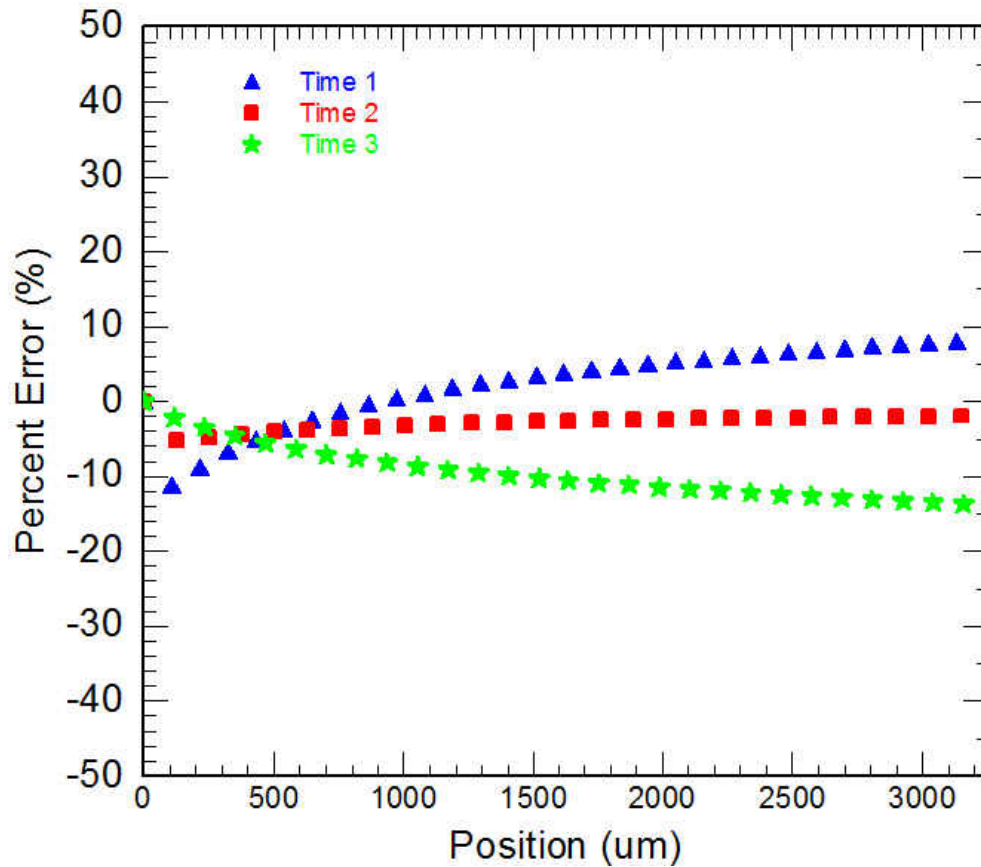
The difference between the 450 nm measurements and the 656 nm were extremely close along the entire meniscus measurement process. The average errors between the two measurements were calculated according to the 656 nm measurement and were found to be equal to or less than 10% (Err$_{t=0}$ = -2.85%, Err$_{t=90min}$ = -2.83%, Err$_{t=180min}$ = -10.21%). The errors by positon were then plotted together to show that the maximum error never exceeds 15% which would deem the steady state condition questionable (Fig. 24).

Figure 24: Percent error vs. position. Error plot represents the difference between the 450 nm measurement at 656 nm measurement for individual test times (Time 1 = 0, Time 2 = 90 min, Time 3 = 180 min).

By plotting the averages of each film together (Fig 25), the steady state assumption can be proved.

During the 90 minutes between measurements 1-2, the ambient air was cooled by the building air

conditioning unit and this increased the meniscus volume as the evaporative mass flux decreased.

After the second measurement was taken the room was allowed to warm up to the initial state of

21°C which resulted in higher evaporation and a decrease in film volume.
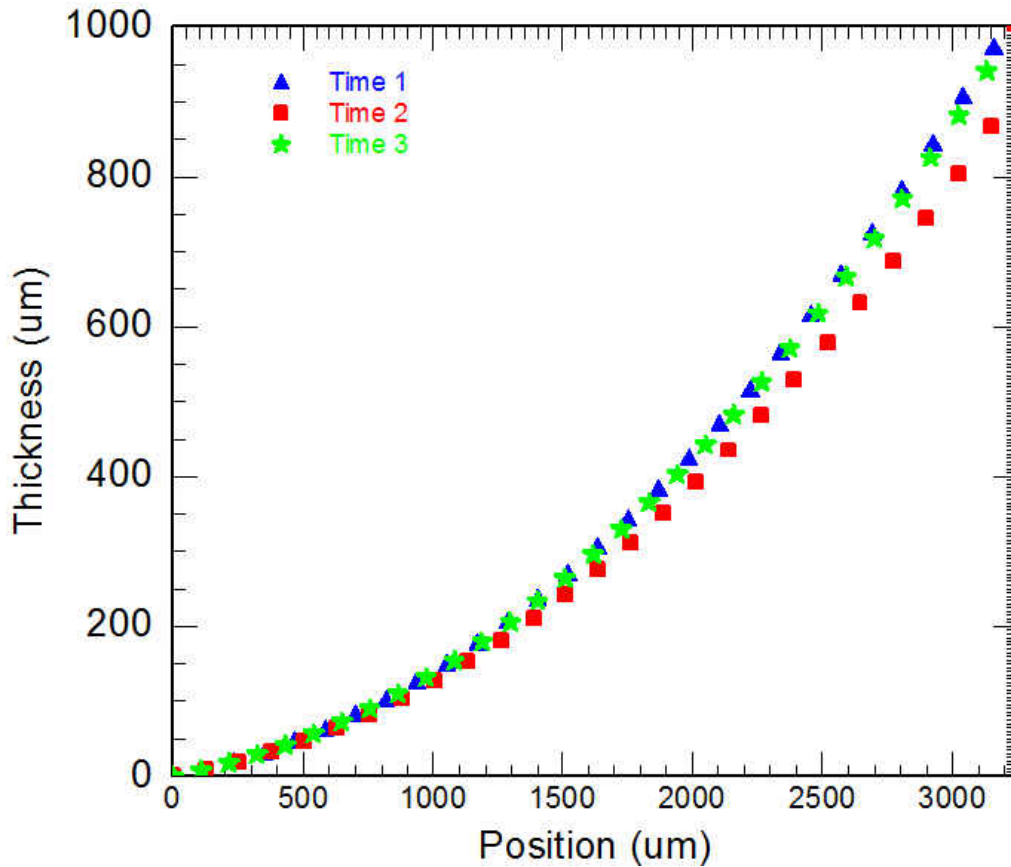
Figure 25: Meniscus thickness (δ) vs. position for H$_2$O film at flow rate 25 nL/s

Steady state can be said to be achieved and the results for the meniscus profile are confirmed as

the position of the contact line was 3.25 mm from the inner corner of the meniscus. The plot shows

the film reaching the wall at approximately 3.25 mm confirming the value of x_o = 3.25 mm. As

the calculated value of the x_o matches the known constraints of the problem ($\delta(x_o)$ = 1 mm).

For a film with a small thin film region, such as this one, where water is evaporating

extremely slow, large curvatures in the thin film region are unlikely to naturally exist. After

calculating the curvature as a function of position, curvatures were observed to decrease over

distance as the film transitions from disjoining pressure dominate conditions to capillary force dominate conditions (Fig. 26).
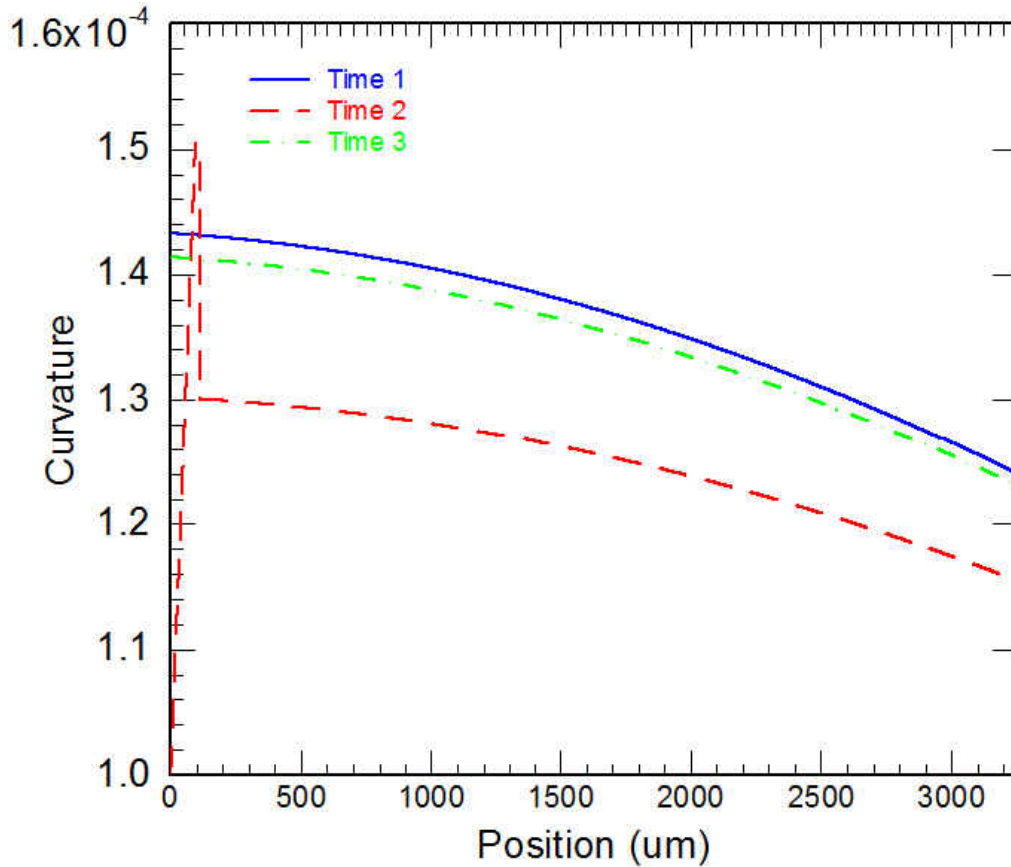
Figure 26: Curvature (K) vs. Position for a steady state H$_2$O film at flow rate 25nL/s

The curvature for all three films vary slightly but the overall structure and rate of change of the curvatures are very consistent so it can be concluded that the films are very steady in their structure and curvature even with the small temperature change experienced by the room.

Conclusion

As previously discuss, steady state conditions are incredibly hard to achieve and take considerable amount of time to build. The unsteady nature of a thin film is still under investigation

and results of this experiment can be considered a great new addition to this ongoing investigation. As films decrease in volume, combining with other effects of contact line with draw or pinning, the thin film region can be stretched, therefore further increasing the evaporative mass flux and volume of the film. This can result in runaway evaporation leading to complete dry out of part. To ensure this did not happen measures were taken to control the recession of the contact line until contact line rescission was seen to be naturally halted. As the film was seen to be unmoving for 3 hours (constrained by syringe volume), steady state conditions can be said to be almost achieved if not for the temperature fluctuations during the measurement process. All values of thickness, curvature, and errors were within realistic and expected values meaning the experiment itself is a great step toward new exciting investigations in which a steady state film is desired. The next step of this experiment entails the addition of a hydrogel layer, extensively discussed previously, to potentially elongate the thin film meniscus region and therefore increase the overall evaporative mass flux.

CHAPTER 5: FUTURE WORK AND MODIFICATIONS

The work detailed in this thesis is only the beginning to a very extensive study of the thin film meniscus and its associated heat transfer properties. In future experiments using this set up, Hydrogel coatings and their effects on meniscus curvature and evaporation rates can be studied. Also, a heating plate will be used to observe the film at several different temperatures ranging from 25ºC to 70ºC. This will give a more complete view of the heat transfer and evaporation rates as this experiment only deals with evaporation at 20ºC. By increasing the temperature, the surface tension dependency on temperature can be studied along with associate temperature dependencies on curvature. By varying the temperature of the heating plate additional global reactions of the thin film regime will be captured and thus providing an even deeper analysis into this nanoscale region.

To get a local view of heat transfer coefficient of the thin film meniscus, a method of pumping heat into a very small area beneath the film and using a laser to measure the temperature of the region moments after the heat addition process can be used. The use of anisotropic time domain thermos-reflectance (TDTR) [23], discussed earlier, will give a localized analysis of the heat transfer coefficient of the thin film region at various points along the meniscus.

With the use of numerical models, computational fluid dynamics, and experimental data, an accurate depiction of the physical phenomena taking place in this ultrathin region will be constructed. The combination of these two processes, heating plate and TDTR, will provide an extension to this work and as complete of an experimental data set as possible to be used in the search for the understanding of this small, yet very important, heat transfer regime.

REFERENCES

[1]   H. Wang, Z. Pan, and Z. Chen, "Thin-liquid-film evaporation at contact line," *Front. Energy Power Eng. China*, vol. 3, no. 2, pp. 141–151, 2009.

[2]   T. Young, "An Essay on the Cohesion of Fluids," *Philos. Trans. R. Soc. London*, vol. 95, no. 0, pp. 65–87, 1805.

[3]   Y. Yuan and T. R. Lee, "Contact Angle and Wetting Properties," in *Surface Science Techniques*, vol. 51, no. 1, 2013, pp. 3–5.

[4]   V. Sobolev, N. Churaev, M. Velarde, and Z. Zorin, "Surface Tension and Dynamic Contact Angle of Water in Thin Quartz Capillaries.," *J. Colloid Interface Sci.*, vol. 222, no. 1, pp. 51–54, 2000.

[5]   S. Shibuichi, T. Onda, N. Satoh, and K. Tsujii, "Super Water-repellent Surfaces Resulting from Fractal Structure," *J. Phys. Chem.*, vol. 100, pp. 19512–19517, 1996.

[6]   J. Bico, U. Thiele, and D. Quéré, "Wetting of textured surfaces," in *Colloids and Surfaces A: Physicochemical and Engineering Aspects*, 2002, vol. 206, no. 1–3, pp. 41–46.

[7]   D. Öner and T. J. McCarthy, "Ultrahydrophobic surfaces. Effects of topography length scales on wettability," *Langmuir*, vol. 16, no. 20, pp. 7777–7782, 2000.

[8]   J. Kim, M.-W. Moon, and H.-Y. Kim, "Dynamics of hemiwicking," *J. Fluid Mech.*, vol. 800, pp. 57–71, 2016.

[9]   C. Ishino, M. Reyssat, E. Reyssat, K. Okumura, and D. Quéré, "Wicking within forests of micropillars," *Europhys. Lett.*, vol. 79, no. 5, p. 56005, 2007.

[10]   H. Wang, S. V. Garimella, and J. Y. Murthy, "An analytical solution for the total heat transfer in the thin-film region of an evaporating meniscus," *Int. J. Heat Mass Transf.*, vol. 51, no. 25–26, pp. 6317–6322, 2008.

[11]   S. S. Panchamgam, S. J. Gokhale, J. L. Plawsky, S. DasGupta, and P. C. Wayner, "Experimental Determination of the Effect of Disjoining Pressure on Shear in the Contact Line Region of a Moving Evaporating Thin Film," *J. Heat Transfer*, vol. 127, no. 3, pp. 231–243, 2005.

[12]   H. Hu and R. G. Larson, "Marangoni effect reverses coffee-ring depositions," *J. Phys. Chem. B*, vol. 110, no. 14, pp. 7090–7094, 2006.

[13]   P. J. Sáenz, P. Valluri, K. Sefiane, and O. K. Matar, "Stability and Two-phase Dynamics of Evaporating Marangoni-driven Flows in Laterally-heated Liquid Layers and Sessile Droplets," *Procedia IUTAM*, vol. 15, pp. 116–123, 2015.

[14]   D. DeRossi, K. Kajiwara, Y. Osada, and A. Yamauchi, *Polymer Gels: Fundamentals and Biomedical Applications*, vol. 53. 1991.

[15]   Y. Tanaka, J. P. Gong, and Y. Osada, "Novel hydrogels with excellent mechanical performance," *Prog. Polym. Sci.*, vol. 30, no. 1, pp. 1–9, 2005.

[16]   Y. Tanaka, K. Fukao, and Y. Miyamoto, "Fracture energy of gels," *Eur. Phys. J. E. Soft Matter*, vol. 401, no. 3, pp. 395–401, 2000.

[17]   D. Bonn, H. Kellay, M. Prochnow, K. Ben-Djemiaa, and J. Meunier, "Delayed Fracture Of An Inhomogeneous Soft Solid," *Science (80-.).*, vol. 280, no. 5361, pp. 265–267, 1998.

[18]   J. Zarzycki, "Critical stress intensity factors of wet gels," *J. Non. Cryst. Solids*, vol. 100, no. 1–3, pp. 359–363, 1988.

[19]   J. E. Silva *et al.*, "Stick-slip water penetration into capillaries coated with swelling hydrogel.," *Soft Matter*, vol. 11, pp. 5933–5939, 2015.

[20]   T. Kajiya, P. Brunet, L. Royon, A. Daerr, M. Receveur, and L. Limat, "A liquid contact line receding on a soft gel surface: Dip-coating geometry investigation.," *Soft Matter*, vol. 10, no. 44, pp. 8888–8895, 2014.

[21]   T. Kajiya, A. Daerr, T. Narita, L. Royon, F. Lequeux, and L. Limat, "Advancing liquid contact line on visco-elastic gel substrates: stick-slip vs. continuous motions," *Soft Matter*, pp. 454–461, 2013.

[22]   A. Mukherjee and S. G. Kandlikar, "Numerical Study of an Evaporating Meniscus on a Moving Heated Surface," *J. Heat Transfer*, vol. 128, pp. 1285–1292, 2006.

[23]   M. Mehrvand and S. A. Putnam, "Heat transfer coefficient measurements in the thermal boundary layer of microchannel heat sinks," *2016 15th IEEE Intersociety Conference on Thermal and Thermomechanical Phenomena in Electronic Systems (ITherm)*. pp. 487–494, 2016.